nature photonics

Letter

https://doi.org/10.1038/s41566-023-01230-z

# Sensitive near-infrared circularly polarized light detection via non-fullerene acceptor blends

Received: 16 December 2021

Accepted: 3 May 2023

Published online: 8 June 2023

Check for updates

Li Wan [1,4,5] ✉, Rui Zhang [1,5], Eunkyung Cho [2], Hongxiang Li [3], Veaceslav Coropceanu [2], Jean-Luc Brédas [2] & Feng Gao [1] ✉

Circularly polarized light (CPL) is widely used for various applications in sensing and imaging[1–3]. An ongoing challenge is to realize high-quality CPL detection using chiral organic semiconductors, especially in the near-infrared (NIR) region[4]. Chiral molecules tend to rely on twisted stereogenic moieties; however, conventional approaches to reduce the bandgap of organic semiconductors are based on the use of co-planar backbones that commonly lead to molecular symmetries preventing chirality. Here we report a widely applicable strategy to directly induce chiroptical activity in planar non-fullerene acceptors[5–7], which are widely used for high-performance organic photovoltaics and provide a wealth of opportunities to fill the spectral gap of CPL detection in the NIR regime. We demonstrate proof-of-concept circularly polarized organic photodiodes using chiroptically active non-fullerene acceptor blends, which exhibit strong circular dichroism and hence great sensitivity to CPL in the NIR region. Importantly, this strategy is found to be effective in a wide series of state-of-the-art non-fullerene acceptor families including ITIC[5], *o*-IDTBR[6] and Y6 analogues[7], which substantially broadens the range of materials applicable to NIR CPL detection.

Circular polarization of electromagnetic waves has been used in a wide range of applications including satellite communication[8], bioimaging[9] and polarization-enhanced sensing technologies[1]. The basic working principle in circularly polarized light (CPL) photodetectors is the ability to discriminate between left-handed (LH) and right-handed (RH) CPL, which can be quantified by the dissymmetry factor (*g*-factor)[10,11]:

$$g = \frac{I_L - I_R}{\frac{1}{2}(I_L + I_R)}, \quad (1)$$

where *I* represents a physical parameter such as absorbance or photocurrent, whereas L/R refers to LH/RH CPL illumination[12].

To translate CPL signals into electrical signals, the sensing wavelength of the photodetector has to match that of the deployed CPL sources. The successful use of a CPL photodetector, thus, requires a rigorous selection of detection wavelengths ($\lambda_{det}$) with the desired high absorption and photocurrent dissymmetry factors ($g_{abs}$ and $g_{ph}$, respectively). Bragg reflective metamaterials have been extensively developed for CPL detection beyond >1,000 nm (ref. 13) and towards the mid-infrared regime, mainly used for satellite communications[14]. Similar working principles apply to liquid-crystal-layer-functionalized

[1]Department of Physics, Chemistry and Biology (IFM), Linköping University, Linköping, Sweden. [2]Department of Chemistry and Biochemistry, The University of Arizona, Tucson, AZ, USA. [3]State Key Laboratory of Polymer Physics and Chemistry, Changchun Institute of Applied Chemistry, Chinese Academy of Sciences, Changchun, China. [4]Present address: Max Planck Institute of Microstructure Physics, Halle, Germany. [5]These authors contributed equally: Li Wan, Rui Zhang. ✉e-mail: li.wan@mpi-halle.mpg.de; feng.gao@liu.se

https://doi.org/10.1038/s41566-023-01230-z

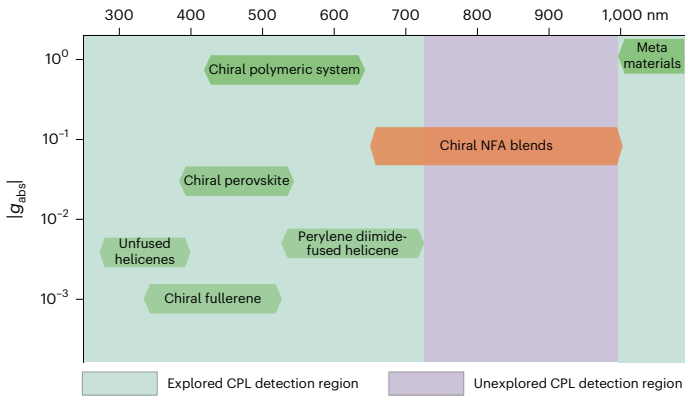


**Fig. 1 | Illustration of systems reported for CPL detection.** Representative highest $|g_{abs}|$ values reported in each group of materials are highlighted along with their CD active region[12,15–20,26,27]. Chiral NFA blends developed in this work (for example, chiral ITIC blends) are able to cover the 650–1,000 nm range for CPL sensing.

devices, where CPL detection relies on selective reflection instead of intrinsic chiroptical response (that is, circular dichroism (CD)). For cost-effective and miniaturized devices for CPL detection, an increasing number of intrinsically chiral organic and hybrid materials have been investigated. For studies reported in this field over the past decade, CPL detection is mainly accessible in the range of 300–650 nm (Fig. 1)[12,15–20].

The key challenge in CPL detection lies in the near-infrared (NIR) region (Fig. 1; Supplementary Table 1 provides a detailed working principle difference)[4,21], which has potential applications in the field of night vision[22] and autonomous vehicles[23]. Although attempts have been made to approach NIR absorption via direct synthesis strategies[24,25], it remains challenging to achieve strong and intrinsic chiroptical activity at the same time (for example, $g_{abs} > 0.1$). To reduce the bandgap of organic compounds and achieve the favoured π–π stacking for efficient charge transport, the material design usually relies on achieving co-planar backbones with large fused aromatic moieties and efficient long-axis charge-transfer-type electronic transitions. Unfortunately, these design strategies are usually not compatible with the emergence of strong chiral activity. From the pioneering work on CPL detectors using chiral side-chain polymers[26] to the most recent chiral perovskites[18–20], materials designs for circularly polarized organic photodiodes (CP-OPDs) were based on developing more twisted molecular structures, whose lowest-energy absorption band peaks can hardly reach 650 nm and beyond[12,15–20,26,27].

An attractive approach to address this dilemma is to make use of the so-called non-fullerene acceptors (NFAs), which are being extensively developed for high-efficiency organic solar cells[5]. Indeed, these NFAs not only show strong absorption peaks up to 1,000 nm (ref. 28) but also display strong intermolecular interactions, which makes it possible to develop chiroptical activities by exploiting exciton coupling among adjacent chromophores, as reported for polyfluorenes[29].

An archetypal NFA, ITIC (Fig. 2a)[5], was selected to demonstrate the emergence of chiroptical activities, on addition of a chiral compound (for example, R5011 (ref. 30); Fig. 2b) that induces a strong excitonic CD with the assistance of the mixed spin-coating solvent. ITIC features a symmetric indacenodithieno[3,2-*b*]-thiophene (IDTT) core and two 1,1-dicyanomethylene-3-indanone (IC) end groups. Its main absorption band at 700 nm consists of a combination of a π–π* IDTT transition and a charge transfer transition from the IDTT core to the IC ends (Supplementary Fig. 1)[31]. When deposited from chloroform (CF), both neat (ITIC) and blend (ITIC:R5011) films exhibit silent CD signals (Fig. 2a and Supplementary Fig. 1) at the ITIC lowest absorption band; the CD spectrum of the blend film only shows a weak signal at $\lambda = 240$ nm (~20 mdeg; Supplementary Fig. 2) corresponding to R5011 absorption (Supplementary Fig. 3), which indicates the absence of any induced CD in the ITIC structures. When a mixed spin-coating solvent is used, for instance, in the presence of 10 vol% chlorobenzene (CB) (Fig. 2a; Supplementary Fig. 4 shows the other solvents), the main absorption band of ITIC becomes broader and slightly redshifts, indicating a larger distribution of electronic states. This is accompanied by the emergence of a strong negative CD signal of approximately −2,000 mdeg ($g_{abs} \approx -0.06 \pm 0.01$) at $\lambda = 706$ nm. The CD spectra show no change subjected to rotation or flip of the thin-film sample (Supplementary Fig. 5), suggesting negligible linear dichroism–linear birefringence effects in the measured CD response[32]. Further optimization of the mixing ratio of the co-solvent (Supplementary Fig. 6), selection of the other co-solvent (Supplementary Fig. 5) and blending ratio of the chiral additives (Supplementary Figs. 4 and 7) result in an optimal $g_{abs}$ value of −0.15 (±0.01) (Supplementary Fig. 7), which is 75-fold larger than that of the very first example of intrinsically chiral organics used for NIR CPL detection[4]. It is worth noting that recent studies have shown that the morphology of many neat or blend NFA films has a strong dependence on the nature of the solvents and additives used for their preparation[33,34].

The $g$ value for an electronic transition in a chiral compound is defined as[35]

$$g = 4\frac{|\mathbf{m}||\boldsymbol{\mu}|}{\mathbf{m}^2 + \boldsymbol{\mu}^2}\cos\theta, \tag{2}$$

where $\mathbf{m}$ and $\boldsymbol{\mu}$ denote the magnetic and electric transition dipoles, respectively, whereas $\theta$ is the angle between them. Since ITIC has a planar backbone conformation and a symmetric structure, the intrinsic molecular rotatory strength $R$ ($|\mathbf{m}||\boldsymbol{\mu}|\cos\theta$) is vanishingly small due to a negligible $|\mathbf{m}|$ value and the orthogonality of $\mathbf{m}$ and $\boldsymbol{\mu}$ (ref. 35). Thus, it can be ruled out that individual ITIC molecules are responsible for the strong chiroptical activity and large rotatory strength observed in the ITIC blends.

Instead, to rationalize the strong CD signals appearing in our samples[36], we need to consider the interchromophoric exciton coupling between adjacent ITIC molecules, as described by equation (3):

$$R_{1,2} \propto \mathbf{r}_{12} \cdot \boldsymbol{\mu}_1 \times \boldsymbol{\mu}_2. \tag{3}$$

Here $R_{1,2}$ describes the rotatory strength in the case of a dimer consisting of two interacting chromophores 1 and 2 with electric transition dipole $\boldsymbol{\mu}_1$ and $\boldsymbol{\mu}_2$, and $\mathbf{r}_{12}$ represents the intermolecular distance vector. As a result of exciton coupling, the magnitude of the dissymmetry factor is no longer restricted by the relative magnitudes of the $\boldsymbol{\mu}$ and $\mathbf{m}$ dipoles of the individual chromophores as in non-excitonically coupled systems[36,37]. The excited states in such coupled chromophores split into non-degenerate levels (that is, Davydov splitting[37]), giving rise to LH and RH CPL absorption[37,38]. We note that the observation of split excited states is consistent with other experimental results reported here, including the broadening of the low-energy absorption band and the appearance of bisignate couplets in the CD spectra (Fig. 1a).

To investigate which moieties drive the chirality induction in ITIC, we separately blend R5011 with the core-unit molecule (that is, IDTT) and the end-group molecule (that is, IC). As shown in Supplementary Figs. 8 and 9, IDTT blend films exhibit no CD signal, whereas IC:R5011 blend films show a new CD peak at ~340 nm corresponding to IC π–π* transitions (Supplementary Fig. 10). This clear difference indicates that it is the IC units that play a dominant role in the formation of chiral configurations in the solid-state ensemble of ITIC molecules. Due to the large steric hindrance of the bulky side chains on the IDTT cores, the π–π stacks of ITIC molecules are predominantly driven by IC–IC interactions owing to the closer spatial and orientational contacts

https://doi.org/10.1038/s41566-023-01230-z

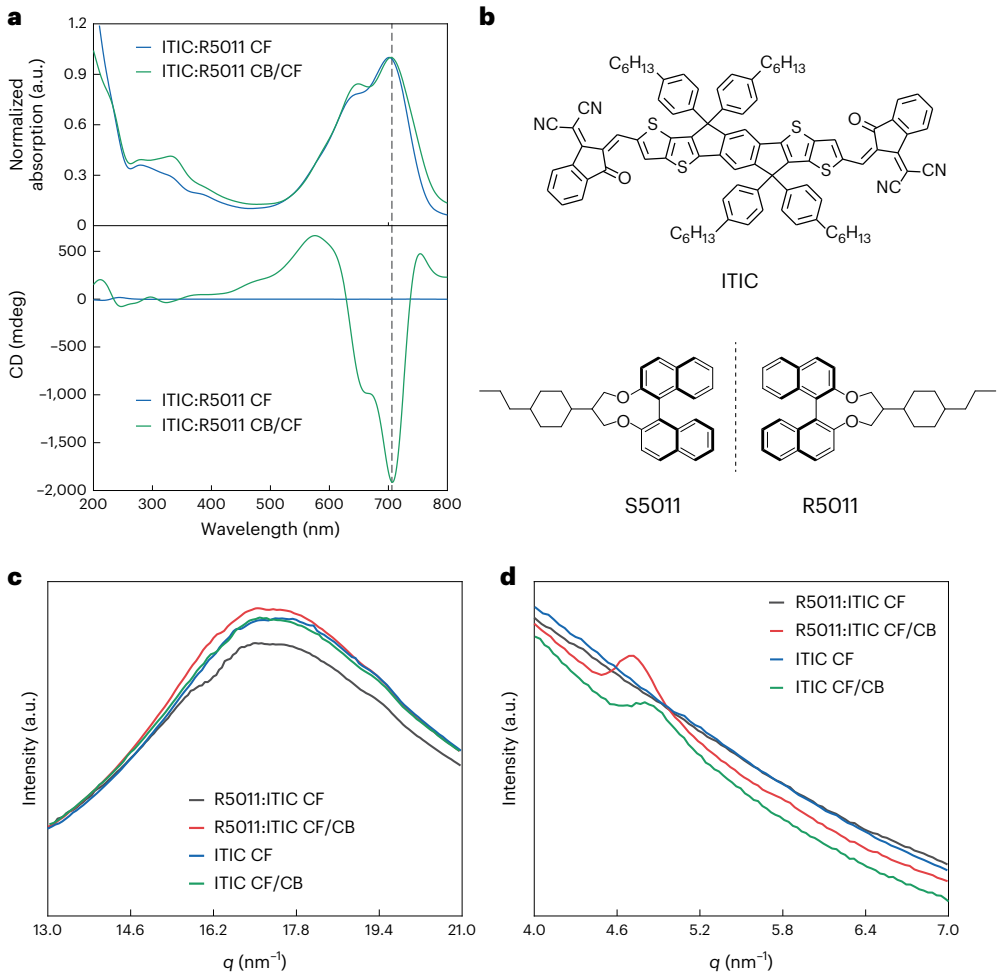


**Fig. 2 | Photophysical characterization of chiral and non-chiral ITIC blend films. a**, Thin-film absorption and CD spectra of R5011:ITIC (10:90 wt%) blends deposited from CF and a CF/CB = 9:1 v/v mixed solvent. **b**, Molecular structures of ITIC and R/S5011. GIWAXS thin-film scattering profiles of neat (ITIC) and blend (ITIC:R5011) films deposited from CF or from CF/CB mixed solvent. **c**, Out-of-plane scattering profile. All the films exhibit an out-of-plane diffraction peak at $q$ = ~17.5 nm$^{-1}$ ($d = 2\pi/q$ = 3.59 Å). **d**, In-plane scattering profile. No obvious diffraction peak is observed for films deposited from the neat CF solvent. When deposited from the mixed solvent, diffraction peaks at $q$ = 4.83 nm$^{-1}$ ($d$ = 13.0 Å) and $q$ = 4.71 nm$^{-1}$ ($d$ = 13.3 Å) can be observed for the neat and blend ITIC films, respectively.

(Supplementary Fig. 8)[39]. Thus, when the π–π-stacking motifs across IC moieties are perturbed by the chiral additive, the entire NFA ensemble is then driven into a chiral configuration, similar to the 'sergeants and soldiers' effect observed in chiral polymer assemblies[40].

Since exciton coupling in ITIC (occurring through IC intermolecular interactions) is evident from the spectroscopic analysis, it is informative to visualize such chromophoric interactions at the level of polycrystalline thin films. Using two-dimensional (2D) grazing-incidence wide-angle X-ray scattering (GIWAXS), we probed the morphological information associated with the induced CD, to capture the three-dimensional packing structures in the chiral ITIC blends. As shown in Fig. 2c and Supplementary Fig. 11 (2D patterns), all the neat and blend films exhibit almost identical ITIC π–π-stacked (010) diffraction signals in the out-of-plane direction. Compared with the films deposited from CF, when spin coated from the mixed solvent, the neat ITIC films exhibit a slightly more ordered in-plane structure with a diffraction peak at $q$ = 4.83 nm$^{-1}$ (Fig. 2d)[41]. This is consistent with the reported GIWAXS patterns, where a mesh-like structure is formed[33], featuring continuous aromatic structures separated by aliphatic domains. On the incorporation of chiral additives, a more ordered in-plane structure is formed with increased molecular separation, indicating a reorientation of the ITIC assemblies.

The absence of disrupted π–π stacks confirms our previous spectroscopic observation, that is, the coupled CD originates in the exciton coupling of rotated ITIC chromophores instead of twisted backbones. Next, we discuss—with the help of time-dependent density functional theory (DFT) calculations—how the three-dimensional assembly of ITIC chromophores amplifies the chiroptical response and results in increased separations within the aromatic–aliphatic–aromatic (lamellar) packing structure.

We start with symmetric ITIC monomers, taken from an experimental crystal structure[42] or optimized at the DFT level. As expected, these monomers exhibit zero rotatory strength ($R$) and $g$-factor (Supplementary Fig. 12 and Supplementary Table 2). Twisting the molecules to generate a helical structure has only a minor effect on the calculated $g$-factors (Supplementary Fig. 13 and Supplementary Table 3); we recall that distorting the planarity of the molecules would impact the structure of the ITIC π stacks driven by the packing of the IC end groups[39], which would contradict the GIWAXS results. Thus, intramolecular twisting can be reasonably ruled out as the dominant contribution to the induced chirality.

When considering ITIC dimers, although optimized collinear dimers with no in-plane rotations between individual monomers exhibit zero $R$ as expected, the appearance of in-plane rotation angles

https://doi.org/10.1038/s41566-023-01230-z

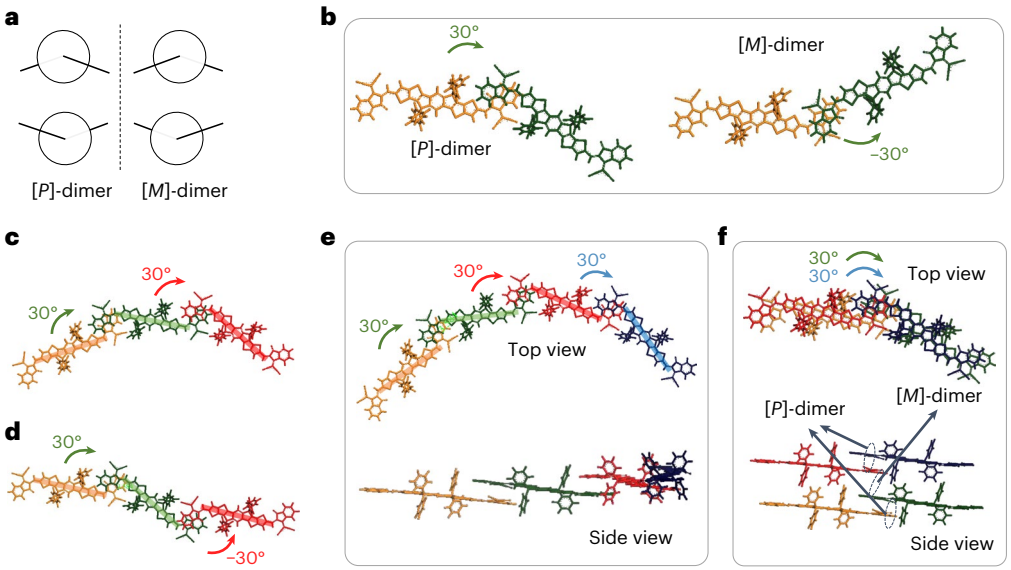


**Fig. 3 | Schematic of the formation of chiral ITIC assemblies. a**, [*P*] and [*M*] conventions used in this work to describe the stereochemistry of intermolecular orientations. The molecular backbones are simplified as the solid lines. **b**–**d**, Molecular orientations of [*P*]-/[*M*]-dimers (**b**), [*P*,*P*]-trimers (**c**) and [*P*,*M*]-trimers (**d**). The top and side views of the molecular orientations in a tetramer comprising two [*P*]-dimers (yellow–green pair and red–dark blue pair). **e**,**f**, For the sake of clarity, a [*P*,*P*,*P*]-tetramer is used to describe ITIC stacks with successive in-plane rotations of chains (**e**), whereas a [*P*]–[*M*]–[*P*]-tetramer is used to describe the assembly of two [*P*]-dimers along the ITIC π–π stack (**f**).

between the ITIC molecules has a substantial impact on the chiroptical response (Supplementary Figs. 14 and 15 and Supplementary Tables 4 and 5), as it yields an intermolecular helical structure. To provide a clear stereochemistry description of the ITIC assemblies, we define the [*P*] and [*M*] geometries of the ITIC dimers according to the molecular orientations depicted in Fig. 3a. Given that [*P*]- and [*M*]-dimers generated by ±30° rotations exhibit equal and opposite *g*-factors (Fig. 3b, Supplementary Fig. 16 and Supplementary Table 6), we hereafter focus on [*P*]-enantiomers in larger ITIC assemblies. We note that the molecules successively stacked with the same direction of rotation form enantiomerically pure trimers (Fig. 3c), whereas zigzag-shaped shape [*P*,*M*]-trimers exhibit negligible *g*-factors (Fig. 3d and Table 1). Increasing the number of ITIC molecules in enantiomerically pure stacks results in a *g*-factor amplification from $8 \times 10^{-4}$ (dimers; Fig. 3b) to $2.6 \times 10^{-3}$ (tetramer; Fig. 3e and Table 1). Both tetramers assembled through continuous in-plane rotation and out-of-plane stack of two [*P*]-dimers exhibit improved positive *g*-factors (Fig. 3e,f), indicating that the promotion of one enantiomeric π stack perturbed by chiral additives is the prerequisite for the enhanced *g*-factors[43] (Supplementary Figs. 17 and 18 and Supplementary Tables 7 and 8).

In chiral ITIC blends, ITIC molecules are assembled either in the chiral configuration (for example, [*M*,*M*]-trimers) or achiral configuration (for example, [*P*,*M*]-trimers; Supplementary Fig. 19). To explain the increased in-plane displacement (Fig. 2d), we now consider a simplified scenario where chiral [*M*,*M*] fragments are embedded in zigzag achiral [*P*,*M*]-trimers with fixed out-of-plane displacement (Supplementary Fig. 20). By sharing one ITIC chain, the chiral [*M*,*M*]-trimers can be attached to two achiral [*P*,*M*]-trimers (black fragments). If one of the [*M*,*M*]-trimers (for example, brown fragments) exhibits an angular ITIC stack in a clockwise manner, the other trimer (for example, dark blue fragments) rotates anticlockwise. Other achiral or chiral fragments can be connected to both the free ends of the [*M*,*M*]-trimers to form further uninterrupted π stacks bridged by the IC–IC interaction. Owing to the statistically appearing branched shape observed from the top view of the chiral assemblies (Supplementary Fig. 21) and associated additional hindrance, the chiral-fragment-embedded ITIC chains are expected to exhibit a larger in-plain displacement. We remark that in a spin-coated film, the packing structures of crystalline and non-crystalline sites of ITICs are more complicated and harder to predict, thus exhausting all the possible chiral assemblies, and this is beyond the scope of this study. However, we believe our proposed structure based on planar ITIC chains would inspire further theoretical studies on the solid-state packing of a strongly chiroptically active π-conjugated system.

The strong CD of the ITIC:R/S5011 blends motivated us to develop an active layer for CP-OPDs, where a donor polymer PBDBT[44] is added to form a bulk heterojunction. The optimized ternary blends based on R5011 and S5011 exhibit mirror CD images and a slightly reduced signal of ~3,000 mdeg ($|g_{abs}| \approx 0.09$; Supplementary Figs. 22 and 23 show the detailed optimization), compared with their binary counterparts (CD ≈ 4,000 mdeg and $|g_{abs}| \approx 0.15$ at $\lambda = 704$ nm; Fig. 4a), which is possibly due to the tail absorption of PBDBT at ~700 nm and perturbation of the interactions between the ITIC molecules and the chiral additives caused by PBDBT.

Proof-of-concept CP-OPDs were fabricated using a device structure of indium tin oxide/PEDOT:PSS/R5011:ITIC:PBDBT/PDINO/Al (see the 'OPD fabrication and characterization' section for more details), where PDINO was selected as the electron transport layer (Supplementary Fig. 24)[45]. The dark current of our CP-OPD is $2.33 \times 10^{-11}$ A (at 0 V; Fig. 4b), which is comparable with the CP-OPDs reported so far[16,26]. On illumination at $\lambda = 700$ nm, R5011 blend devices show a linear response from 0.84 nW to 5 μW, which corresponds to a linear dynamic range (LDR) of ~76 dB (at 0 V; Fig. 4c). To evaluate the lowest detectable limit of our CP-OPD, we performed the dark-current noise measurement and calculated the noise-equivalent power. At 0 V bias, the R5011 device exhibits a low noise current level, ranging from ~2.02 to ~6.48 fA $Hz^{-1/2}$, as measured from 1 to 10 Hz. Based on the external quantum efficiency spectra (Supplementary Fig. 24), spectra responsivity (Supplementary Fig. 25) and measured noise (Fig. 4e), we evaluate the noise-equivalent power to be ~$2.0 \times 10^{-14}$ W $Hz^{-1/2}$. We achieved a 700 nm $D^*$ of 1.04 (±0.03) × $10^{13}$ Jones and peak $D^*$ of 1.07 (±0.05) × $10^{13}$ Jones at 730 nm, which is among the highest reported value for CP-OPDs (Supplementary Table 9).

Under a 700 nm square-wave-modulated illumination, the R5011 device demonstrates an average rise/fall time of ~3.48 μs

https://doi.org/10.1038/s41566-023-01230-z

**Table 1 | Calculated chiroptical properties for the given electronic transitions in the ITIC assemblies depicted in Fig. 3**

| Molecular orientation | Dominant electronic transition | $E$ (eV) | $E$ (nm) | $f^a$ | $\|\mu\|$ ($10^{-20}$ esu cm) | $\|m\|$ ($10^{-20}$ erg G$^{-1}$) | cos($\theta^b$) | $R$ ($10^{-40}$ erg esu cm G$^{-1}$) | $g$ |
|---|---|---|---|---|---|---|---|---|---|
| [*P*]-dimer | $S_0 \rightarrow S_2$ | 1.87 | 662 | 4.45 | 2,501 | 3.91 | 0.12 | 1,194 | 0.0008 |
| [*P*,*P*]-trimer | $S_0 \rightarrow S_1$ | 1.82 | 681 | 5.58 | 2,843 | 12.2 | 0.09 | 3,102 | 0.0015 |
| [*P*,*M*]-trimer | $S_0 \rightarrow S_3$ | 1.84 | 674 | 6.02 | 2,938 | 11.1 | −0.01 | −190 | −0.0001 |
| [*P*,*P*,*P*]-tetramer | $S_0 \rightarrow S_1$ | 1.81 | 687 | 7.20 | 3,243 | 25.0 | 0.08 | 6,766 | 0.0026 |
| [*P*]–[*M*]–[*P*]- tetramer | $S_0 \rightarrow S_8$ | 1.91 | 649 | 4.37 | 2,457 | 8.08 | 0.18 | 3,614 | 0.0024 |

[a]Oscillator strength of the electronic transition. [b]Angle between **μ** and **m**.

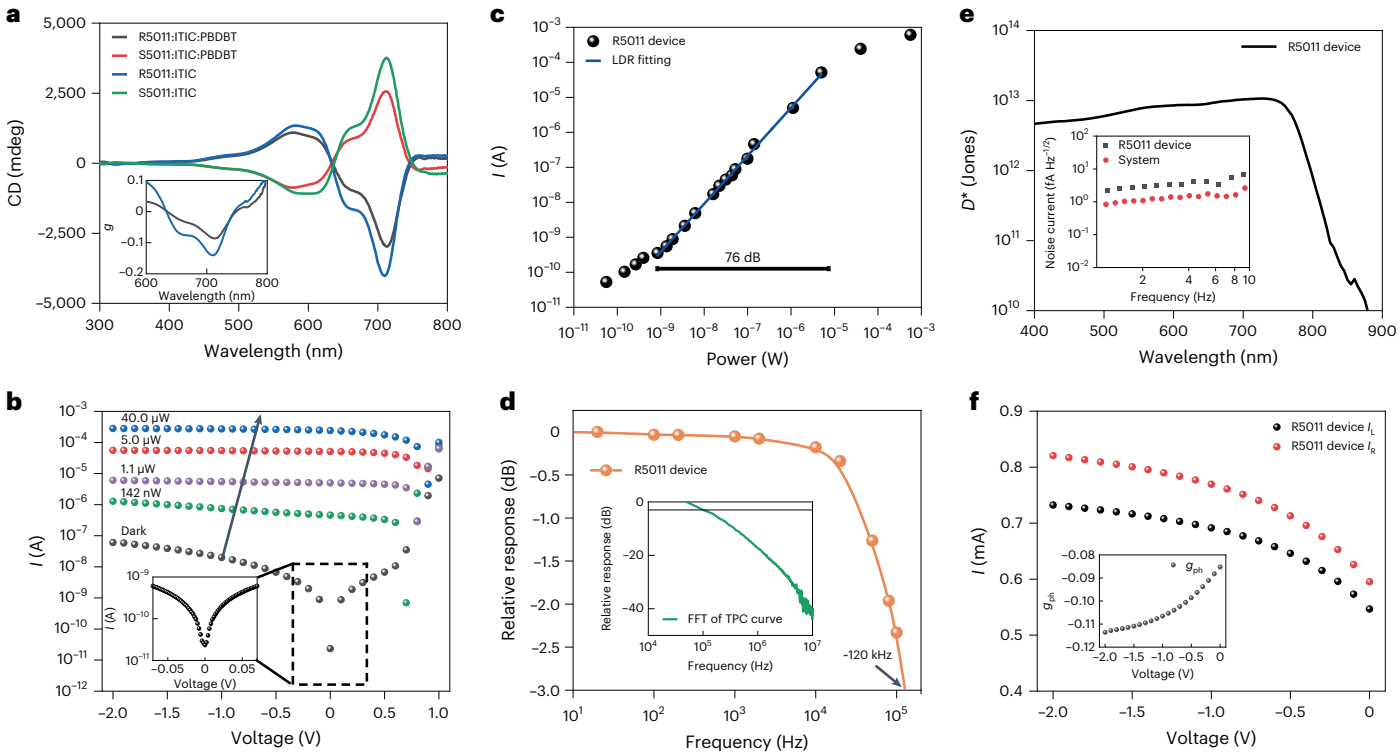


**Fig. 4 | Photodiode characteristics of CP-OPDs based on chiral ITIC blends. a**, CD spectra of binary blend (R/S5011:ITIC = 40:60 wt%) and ternary blend (R/S5011) thin films (R/S5011:ITIC:PBDBT = 40:60:60 wt%) deposited from CF/CB = 9:1 mixed solvent. The inset shows the extracted $g_{abs}$ values. **b**, *J*–*V* characteristics of the R5011 blend OPD, recorded in the dark and under unpolarized illumination with increasing light intensity. The inset shows a detailed curve from −0.005 to 0.005 V. **c**, Linear dynamic range of R5011:ITIC:PBDBT CP-OPD, measured at 0 V. **d**, Frequency response of R5011:ITIC:PBDBT CP-OPD to the 700 nm LED (~110 μW), measured at 0 V. The inset shows the fast Fourier transform (FFT) of the transient photocurrent (TPC) curve. **e**, Calculated specific detectivity of R5011:ITIC:PBDBT CP-OPD, measured at 0 V. The inset shows the system and photodiode noise current. **f**, Photocurrent of R5011:ITIC:PBDBT CP-OPD recorded under illumination of LH and RH CPL (700 nm, ~1 mW).

(Supplementary Fig. 26). The decay of the device response driven by sinusoidal signals with different frequencies was then investigated, and the bandwidth calculated is comparable, reaching as high as ~120 kHz (Fig. 4d). This result is consistent with the fast-Fourier-transformed transient photocurrent curve (Supplementary Fig. 27), demonstrating the fastest response time among the reported CP-OPDs (Supplementary Table 9 lists a comparison).

In terms of CPL sensitivity, the R5011 blend device exhibits photocurrents $I_L$ and $I_R$ of 0.55 and 0.60 mA (at 0 V; Fig. 4e) under the illumination of LH and RH CPL, respectively. The extracted $g_{ph}$ value is slightly amplified up to −0.113, when increasing the bias up to −2.0 V. The average $g_{ph}$ value at 0 V for R5011 and S5011 devices is −0.094 (±0.005) and +0.092 (±0.007), respectively, consistent with real-time measurements, which is almost one order of magnitude larger than the very first example of NIR CP photodetector reported using an intrinsically chiral active layer (Supplementary Figs. 28 and 29)[4]. These results indicate that chiral additives can effectively functionalize ITIC-based active layers for OPDs showing great sensitivity towards CPL signals at 700 nm (Supplementary Table 9 lists the CPL detection at different wavelengths), without imposing any detrimental effect on device performance as an unpolarized OPD.

We are also able to demonstrate that our strategy is generally applicable to other types of state-of-the-art NFAs, such as *o*-IDTBR[6], IEICO[46] and Y18 (ref. 47) (Supplementary Fig. 30 shows the spectra and Supplementary Figs. 31 and 32 show the selective device performance). The CD bands of these systems can be tuned from 600 to 1,000 nm via modifications of the chemical structures. As such, our approach provides an effective way to fill the gap in the detection wavelength of existing chiral systems (Fig. 1).

In summary, we have described an effective strategy to induce strong CD in thin films based on NFAs by making use of strong excitonic coupling between adjacent NFA molecules. Owing to the strong π–π interactions among chromophores in NFA stacks, notable bisignate CD bands can appear, even though the individual NFA molecules are intrinsically achiral. CP-OPDs whose active layers incorporate these chiral assemblies display a large chiroptical response in the NIR region ($g_{abs} > 0.1$), a region that is traditionally inaccessible to other organic semiconductors, which enables efficient CPL sensing in this range. We believe that such strong CP selectivity in the NIR regime, coupled with state-of-the-art response time and specific detectivity, has great potential to transform many real-world sensing and data transmission applications. In addition, our combined experimental and theoretical investigation provides a powerful tool to describe the molecular assemblies critical to chiroptical activities, from the chromophore interactions in dimers to the macroscopic scale.

## Online content

Any methods, additional references, Nature Portfolio reporting summaries, source data, extended data, supplementary information, acknowledgements, peer review information; details of author contributions and competing interests; and statements of data and code availability are available at https://doi.org/10.1038/s41566-023-01230-z.

## References


1. van der Laan, J. D., Scrymgeour, D. A., Kemme, S. A. & Dereniak, E. L. Detection range enhancement using circularly polarized light in scattering environments for infrared wavelengths. *Appl. Opt.* **54**, 2266–2274 (2015).
2. Ding, Y. & Pau, S. Circularly and elliptically polarized light under water and the Umov effect. *Light: Sci. Appl.* **8**, 32 (2019).
3. Crassous, J. et al. Materials for chiral light control. *Nat. Rev. Mater.* https://doi.org/10.1038/s41578-023-00543-3 (2023).
4. Zhang, L. et al. π-Extended perylene diimide double-heterohelicenes as ambipolar organic semiconductors for broadband circularly polarized light detection. *Nat. Commun.* **12**, 142 (2021).
5. Lin, Y. et al. An electron acceptor challenging fullerenes for efficient polymer solar cells. *Adv. Mater.* **27**, 1170–1174 (2015).
6. Holliday, S. et al. High-efficiency and air-stable P3HT-based polymer solar cells with a new non-fullerene acceptor. *Nat. Commun.* **7**, 11585 (2016).
7. Yuan, J. et al. Single-junction organic solar cell with over 15% efficiency using fused-ring acceptor with electron-deficient core. *Joule* **3**, 1140–1151 (2019).
8. Bee Yen, T., Cahill, R. & Fusco, V. F. Understanding and measuring circular polarization. *IEEE Trans. Educ.* **46**, 313–318 (2003).
9. Heffern, M. C., Matosziuk, L. M. & Meade, T. J. Lanthanide probes for bioresponsive imaging. *Chem. Rev.* **114**, 4496–4539 (2014).
10. Wan, L. et al. Inverting the handedness of circularly polarized luminescence from light-emitting polymers using film thickness. *ACS Nano* **13**, 8099–8105 (2019).
11. Wan, L., Liu, Y., Fuchter, M. J. & Yan, B. Anomalous circularly polarized light emission in organic light-emitting diodes caused by orbital–momentum locking. *Nat. Photon.* **17**, 193–199 (2023).
12. Schulz, M. et al. Chiral excitonic organic photodiodes for direct detection of circular polarized light. *Adv. Funct. Mater.* **29**, 1900684 (2019).
13. Li, W. et al. Circularly polarized light detection with hot electrons in chiral plasmonic metamaterials. *Nat. Commun.* **6**, 8379 (2015).
14. Wang, Y. et al. Strong circular dichroism enhancement by plasmonic coupling between graphene and h-shaped chiral nanostructure. *Opt. Express* **27**, 33869–33879 (2019).
15. Shi, W. et al. Fullerene desymmetrization as a means to achieve single-enantiomer electron acceptors with maximized chiroptical responsiveness. *Adv. Mater.* **33**, 2004115 (2021).
16. Ward, M. D. et al. Highly selective high-speed circularly polarized photodiodes based on π-conjugated polymers. *Adv. Opt. Mater.* **10**, 2101044 (2021).
17. Kim, N. Y. et al. Chiroptical-conjugated polymer/chiral small molecule hybrid thin films for circularly polarized light-detecting heterojunction devices. *Adv. Funct. Mater.* **29**, 1808668 (2019).
18. Ishii, A. & Miyasaka, T. Direct detection of circular polarized light in helical 1D perovskite-based photodiode. *Sci. Adv.* **6**, eabd3274 (2020).
19. Li, D. et al. Chiral lead-free hybrid perovskites for self-powered circularly polarized light detection. *Angew. Chem. Int. Ed.* **60**, 8415–8418 (2021).
20. Wang, L. et al. A chiral reduced-dimension perovskite for an efficient flexible circularly polarized light photodetector. *Angew. Chem. Int. Ed.* **59**, 6442–6450 (2020).
21. Shang, X., Wan, L., Wang, L., Gao, F. & Li, H. Emerging materials for circularly polarized light detection. *J. Mater. Chem. C* **10**, 2400–2410 (2022).
22. Luo, Y., Remillard, J. & Hoetzer, D. Pedestrian detection in near-infrared night vision system. In *2010 IEEE Intelligent Vehicles Symposium* 51–58 (IEEE, 2010).
23. Vargas, J., Alsweiss, S., Toker, O., Razdan, R. & Santos, J. An overview of autonomous vehicles sensors and their vulnerability to weather conditions. *Sensors* **21**, 5397 (2021).
24. Liu, L. et al. Chiral non-fullerene acceptor enriched bulk heterojunctions enable high-performance near-infrared circularly polarized light detection. *Small* **18**, 2202941 (2022).
25. Liu, L., Wei, Z. & Meskers, S. C. J. Semi-transparent, chiral organic photodiodes with incident direction-dependent selectivity for circularly polarized light. *Adv. Mater.* **35**, 2209730 (2023).
26. Gilot, J. et al. Polymer photovoltaic cells sensitive to the circular polarization of light. *Adv. Mater.* **22**, E131–E134 (2010).
27. Yang, Y., da Costa, R. C., Fuchter, M. J. & Campbell, A. J. Circularly polarized light detection by a chiral organic semiconductor transistor. *Nat. Photon.* **7**, 634–638 (2013).
28. Hou, J., Inganas, O., Friend, R. H. & Gao, F. Organic solar cells based on non-fullerene acceptors. *Nat. Mater.* **17**, 119–128 (2018).
29. Wan, L., Shi, X., Wade, J., Campbell, A. J. & Fuchter, M. J. Strongly circularly polarized crystalline and β-phase emission from poly(9,9-dioctylfluorene)-based deep-blue light-emitting diodes. *Adv. Opt. Mater.* **9**, 2100066 (2021).
30. Lee, D.-M., Song, J.-W., Lee, Y.-J., Yu, C.-J. & Kim, J.-H. Control of circularly polarized electroluminescence in induced twist structure of conjugate polymer. *Adv. Mater.* **29**, 1700907 (2017).
31. Hu, L. et al. Chemical reaction between an ITIC electron acceptor and an amine-containing interfacial layer in non-fullerene solar cells. *J. Mater. Chem. A* **6**, 2273–2278 (2018).
32. Schulz, M. et al. Giant intrinsic circular dichroism of prolinol-derived squaraine thin films. *Nat. Commun.* **9**, 2413 (2018).
33. Marina, S. et al. Polymorphism in non-fullerene acceptors based on indacenodithienothiophene. *Adv. Funct. Mater.* **31**, 2103784 (2021).
34. Chen, H., Qu, J., Liu, L., Chen, W. & He, F. Carrier dynamics and morphology regulated by 1,8-diiodooctane in chlorinated nonfullerene polymer solar cells. *J. Phys. Chem. Lett.* **10**, 936–942 (2019).
35. Nakai, Y., Mori, T. & Inoue, Y. Theoretical and experimental studies on circular dichroism of carbo[*n*]helicenes. *J. Phys. Chem. A* **116**, 7372–7385 (2012).

36. Harada, N. Exciton coupled circular dichroic spectroscopy and its application to determination of absolute configuration. (Part 1): chiroptical interaction between two or more identical chromophores. *J. Synth. Org. Chem. Jpn* **41**, 914–924 (1983).
37. Berova, N., Harada, N. & Nakanishi, K. Exciton coupling. in *Encyclopedia of Spectroscopy and Spectrometry* 539–557 (Elsevier, 2017).
38. Duong, S. T. & Fujiki, M. The origin of bisignate circularly polarized luminescence (CPL) spectra from chiral polymer aggregates and molecular camphor: anti-Kasha's rule revealed by CPL excitation (CPLE) spectra. *Polym. Chem.* **8**, 4673–4679 (2017).
39. Han, G., Guo, Y., Ning, L. & Yi, Y. Improving the electron mobility of ITIC by end-group modulation: the role of fluorination and π-extension. *Sol. RRL* **3**, 1800251 (2019).
40. Prins, L. J., Timmerman, P. & Reinhoudt, D. N. Amplification of chirality: the 'sergeants and soldiers' principle applied to dynamic hydrogen-bonded assemblies. *J. Am. Chem. Soc.* **123**, 10153–10163 (2001).
41. Liu, X. et al. A high dielectric constant non-fullerene acceptor for efficient bulk-heterojunction organic solar cells. *J. Mater. Chem. A* **6**, 395–403 (2018).
42. Han, G., Guo, Y., Song, X., Wang, Y. & Yi, Y. Terminal π–π stacking determines three-dimensional molecular packing and isotropic charge transport in an A–π–A electron acceptor for non-fullerene organic solar cells. *J. Mater. Chem. C* **5**, 4852–4857 (2017).
43. van Gestel, J. Amplification of chirality of the majority-rules type in helical supramolecular polymers: the impact of the presence of achiral monomers. *J. Phys. Chem. B* **110**, 4365–4370 (2006).
44. Zhao, W. et al. Fullerene-free polymer solar cells with over 11% efficiency and excellent thermal stability. *Adv. Mater.* **28**, 4734–4739 (2016).
45. Zhang, Z.-G. et al. Perylene diimides: a thickness-insensitive cathode interlayer for high performance polymer solar cells. *Energy Environ. Sci.* **7**, 1966–1973 (2014).
46. Yao, H. et al. Design and synthesis of a low bandgap small molecule acceptor for efficient polymer solar cells. *Adv. Mater.* **28**, 8283–8287 (2016).
47. Zhang, C. et al. A disorder-free conformation boosts phonon and charge transfer in an electron-deficient-core-based non-fullerene acceptor. *J. Mater. Chem. A* **8**, 8566–8574 (2020).

# Methods

## Materials

Chiral additives R/S5011 were purchased from Nanjing Sanjiang Advanced Materials R&D. All the NFAs and PBDBT were purchased from Solarmer Materials. All the materials were used without further purification.

### Solution preparation and thin-film deposition

ITIC and R5011 were dissolved in neat CF and CF/CB mixed solvent to a concentration of 20 mg ml$^{-1}$ and blend to form a 10 wt% R5011 solution. Thin films were dynamically spin coated at a speed of 2,000 r.p.m. to give a ~120 nm film and deposited on clean fused silica substrates. The cleaning process for all the substrates involved rinsing in an ultrasonic bath with acetone, isopropyl alcohol, Hellmanex III (Sigma-Aldrich) and deionized water for 15 min. These were followed by an ultraviolet–ozone treatment for 15 min before spin coating. All the samples are measured without annealing and other post-deposition treatments. The thickness of the thin films was controlled by the spin speed and monitored using a DektakXT surface profiler.

### Photophysical and morphological characterizations

The CD spectra and absorption spectra were simultaneously collected using a Chirascan (Applied Photophysics) spectrophotometer. The dissymmetry factor $g_{abs}$ was calculated following the equation $g = (A_L - A_R)/A$, $|g| \leq 2$. The 2D GIWAXS measurements were carried out at the 14BL beamline of the Shanghai Synchrotron Radiation Facility ($\lambda = 1.24$ Å). The sample stage was equipped with a seven-axis motorized stage for the fine alignment of the sample, and the incidence angle of the X-ray beam was set at 0.2 for the neat and blend films. The GIWAXS patterns were recorded with a 2D charge-coupled device detector and an X-ray irradiation time within 100 s, dependent on the saturation level of the detector.

### OPD fabrication and characterization

Prepatterned indium tin oxide glass substrates were sequentially cleaned in an ultrasonic bath with water solution of the surfactant, acetone and isopropanol (15 min each) and dried under a $N_2$ flow before ultraviolet–ozone treatment. PEDOT:PSS (CLEVIOS P VP AI 4083) was spin coated to the indium tin oxide substrates at 2,000 r.p.m. for 60 s. Then, they were immediately transferred to a $N_2$ glovebox. Then, R5011, ITIC and PBDBT were blend in a weight ratio of 4:6:6 in a CB/CF mixed solvent (CB/CF = 10:90 vol%) with a total concentration of 26 mg ml$^{-1}$ and deposited onto the PEDOT:PSS layer to form a ~190 nm film. The film was then annealed at 100 °C for 5 min for better charge transport. PDINO (Ossila) was spin coated onto the active layer at 3,000 r.p.m. from a 0.5 mg ml$^{-1}$ methanol solution. Afterwards, Al was thermally evaporated onto the organic layer under a high vacuum (~$1 \times 10^{-6}$ mbar).

The characterizations of the CP-OPD were carried out under ambient conditions at room temperature. The devices were encapsulated using a drop of ultraviolet adhesive (~5 µl; Norland Products, NOA73) on the metal electrode side of the device and then covered with a glass slide. It was then solidified by illumination with an ultraviolet lamp through the cover glass side for about 15 s.

Current–voltage ($J$–$V$) measurements (device pixel area, 0.047 cm$^2$) were performed using a Keithley 2400 instrument. For measurements under illumination, a mounted light-emitting diode (LED) (Thorlabs, M700L4; 700 nm) was used with a Thorlabs DC2200 driver, which was collimated with an adaptor lens (Thorlabs, SM2F32-A). For measurements of $g_{ph}$, the collimated LED was circularly polarized using an ultrabroadband wire grid polarizer (Thorlabs, WP25M-UB; extinction ratio of >1,000:1 at 700 nm) and a mounted quarter-wave Fresnel rhomb retarder (FR600QM; retardance variation of <2% for 600–1,550 nm). The light intensity was monitored using an ultraviolet-enhanced Si photodetector (Newport; 200–1,100 nm).

The external quantum efficiency and spectra responsivity of the device were measured using a solar-cell spectral response measurement system (QE-R3011, Enli Technology), which was calibrated with a standard Si crystalline solar cell. The dark-current noise spectra of the devices were measured using a lock-in amplifier (SR830, Stanford Research Systems) coupled with a low-noise preamplifier (SR570, Stanford Research Systems), and the device was fixed in a grounded metal box. For Y18 devices, a mounted LED (Thorlabs, M880L3; 880 nm) was used.

The noise-equivalent power NEP and $D^*$ (in Jones) were calculated using the following equations:

$$\mathrm{NEP} = \frac{i_n}{R}, \tag{4}$$

$$D^* = \frac{R\sqrt{A}}{i_n}, \tag{5}$$

where $i_n$ is the dark-current noise (in A Hz$^{-1/2}$), $R$ (in A W$^{-1}$) is the spectra responsivity and $A$ is the area of the device (in cm$^2$). The average $D^*$ is calculated using 16 identical devices.

The weak light response and LDR of the photodetector were carried out by using up to two neutral density filters and a Thorlabs DC2200 LED driver to vary the light power. The output power was calibrated with the Si photodiode. The current signals of the devices were recorded by the Keithley 2400 device. The LDR was calculated using the equation $\mathrm{LDR} = 20\log(P_{high}/P_{low})$, where the subscripts high and low refer to the high and low power limits within the linear-response region of the OPD.

The damping measurements of higher frequency are extracted from the transient photocurrent measurements. The transient photocurrent of the photodetector was measured using an oscilloscope with an input impedance of 50 Ω when the device was excited by a pulse laser (wavelength, 337 nm; pulse width, ~4 ns) from a nitrogen laser (NL100, Stanford Research Systems) after attenuation with a neutral density filter. The rise/fall time and damping (low frequency) measurements were carried out using the LED driver with a 2 kHz square-wave pulse and sinusoidal light with various desired frequencies (<1 MHz).

### DFT calculation and analysis

The ground-state geometries of the monomer and dimer were optimized at the B3LYP/6-311G** level of theory with GD3BJ (D3 with Becke–Johnson damping) dispersion corrections. Time-dependent DFT calculations of the ITIC monomer were carried out at the same level of theory to determine the chiroptical properties of the excited states. In case of the dimer, the hexyl groups attached on the benzene rings in the ground-state-optimized structure were replaced with hydrogen atoms in the time-dependent DFT calculations at the B3LYP/6-31G** level to maintain reasonable computation times. To compare the magnitudes of the electric and magnetic transition dipole moments, the SI units were converted to CGS-Gaussian units, as shown in a previous work[48]. The $g$-factors were obtained from equation (2).

# Data availability

The relevant data are available in the main text and the Supplementary Information. Source data are provided with this paper.

# References

48. Kubo, H. et al. Tuning transition electric and magnetic dipole moments: [7]helicenes showing intense circularly polarized luminescence. *J. Phys. Chem. Lett.* **12**, 686–695 (2021).

# Acknowledgements

L.W., R.Z. and F.G. would like to acknowledge financial support from the Knut and Alice Wallenberg Foundation (Dnr. KAW 2019.0082, F.G.)

and the Swedish Government Strategic Research Area in Materials Science on Functional Materials at Linköping University (faculty grant no. SFO-Mat-LiU #2009-00971, F.G.). F.G. acknowledges the Stiftelsen för Strategisk Forskning through a Future Research Leader programme (FFL18-0322). L.W., R.Z. and F.G. would like to thank the ProLinC facility at LiU for access to the CD spectrometer. L.W., R.Z. and F.G. would like to acknowledge that the GIWAXS measurement was carried out with support from the Shanghai Synchrotron Radiation Facility, 14BL beamline. The work at the University of Arizona was funded by the Office of Naval Research, award no. N00014-20-1-2110 (J.-L.B), and the UA College of Science (V.C. and J.-L.B.).

## Author contributions

L.W. and R.Z. contributed equally to this work. L.W. and F.G. conceived the project. L.W. performed all the spectroscopic measurements. R.Z. fabricated the OPD devices and performed the measurements. H.L. performed the 2D GIWAXS measurement. L.W. and R.Z. further analysed the 2D GIWAXS results. E.C., C.V. and J.-L.B. performed the DFT calculations. L.W. wrote the manuscript. All authors contributed to the discussion of the results and to the edits of the manuscript.

## Funding

Open access funding provided by Linköping University.

## Competing interests

All authors declare no competing interests.

## Additional information

**Supplementary information** The online version contains supplementary material available at https://doi.org/10.1038/s41566-023-01230-z.

**Correspondence and requests for materials** should be addressed to Li Wan or Feng Gao.

**Peer review information** *Nature Photonics* thanks Hanying Li, Longzhen Qiu and the other, anonymous, reviewer(s) for their contribution to the peer review of this work.